Title

Distinct effects of nuclear volume fraction and cell diameter on high b-value diffusion MRI contrast in tumors

Journal

Magnetic Resonance in Medicine, 72(5)

ISSN

0740-3194

Authors

White, Nathan S
Dale, Anders M

Publication Date

2014-11-01

DOI

10.1002/mrm.25039

Peer reviewed

Distinct Effects of Nuclear Volume Fraction and Cell Diameter on High b-Value Diffusion MRI Contrast in Tumors

Nathan S. White[1]* and Anders M. Dale[1,2]

Purpose: While many recent studies have demonstrated improved detection and characterization of malignant lesions using high *b*-value diffusion imaging techniques, little is known about the underlying physical characteristics of tumor cells that modulate the restricted water signal at high *b* on clinical scanners.
Methods: Monte Carlo simulations of diffusion in a synthetic tumor cell environment were used to study the specific effects of tumor cell diameter and nuclear volume fraction (v) on high *b* diffusion contrast.
Results: Results indicate that clinical pulsed-gradient spin-echo diffusion-weighted signals measured at high *b* ($\sim$4000 s/mm^2), long diffusion time (Δ $\sim$40–60 ms), and long echo time (TE $\sim$60–140 ms) are generally insensitive to tumor cell diameter, but increase exponentially with v. Moreover, these results are predicted by a simple analytic expression for the intracellular restricted water signal with elevated T2 for the intranuclear versus cytosolic compartment.
Conclusion: Nuclear volume fraction is an important characteristic of cancer cells that modulates the apparent restriction of water at high *b* on clinical scanners. This model offers a possible explanation for the apparent unreliable correlation between tumor cell density (cellularity) and traditional ADC. **Magn Reson Med 72:1435–1443, 2014. © 2013 Wiley Periodicals, Inc.**

Key words: RSI; restricted diffusion; hindered diffusion; cellularity; conspicuity; stem cells

INTRODUCTION

Noninvasive cancer imaging biomarkers are important tools for the identification and characterization of neoplastic lesions in vivo, as well as for monitoring tumor response to treatment. Owing to the unique sensitivity of proton magnetic resonance signals to the molecular self-diffusion of water at microscopic length scales, diffusion-weighted imaging (DWI) is a powerful tool for probing microstructural and physiological properties of cancer in vivo at the cellular and subcellular level. While the field continues to progress at a rapid pace, the application of DWI as a clinical tool will surely benefit from a deeper understanding of the underlying biological mechanism producing diffusion contrast in both healthy and neoplastic tissue.

In diagnostic oncology, a hallmark radiologic feature of many malignant cancers is elevated DWI signal caused by reduced apparent diffusion coefficient (ADC) of water in the tumor microenvironment (1). While it is generally accepted that reduced ADC in tumors is caused by high packing density of cancer cells in these lesions, the physical mechanism through which this happens remains unclear. In principle, greater cell packing density can reduce ADC through two physical mechanisms. The first is decreased extracellular space volume fraction and increased tortuosity of the extracellular space matrix, which leads to greater diffusion *hindrance* and reduced mobility of extracellular water molecules (2–4). The second is increased intracellular space volume fraction (i.e., cell density) resulting in a greater number of water molecules that are restricted or trapped within the cells themselves (3,4). At long diffusion times (Δ $\sim$30–60 ms) and high diffusion-weighting factors ($b > 3000$ s/mm^2) signal from the hindered yet relatively fast extracellular water compartment is largely attenuated and DWI contrast is dominated by the slow intracellular restricted water signal (4). Building on this phenomenon, many recent studies have demonstrated improved tumor contrast-to-noise (i.e. conspicuity) utilizing DWI data at high *b* through reduced sensitivity to extracellular edema and necrosis (5–8). However, the restricted water signal magnitude remains highly variable both within and across different tumor types in a manner that cannot be explained by cell density alone. One case in point is the lack of restricted signal on DWI in some cell-rich cancers such as oligoastrocytoma. This suggests that the intrinsic properties of cancer cells themselves must also be modulating the apparent restriction of water in tumors, but it is presently unclear what properties of the cancer cells are at play and how these properties modulate diffusion contrast at high *b*.

Two distinguishing morphological characteristics of malignant cancer cells are their large size variations and elevated nuclear volume fractions compared with healthy cells (9). The goal of this study, therefore, was to investigate the specific role of these two physical parameters on the restricted intracellular signal as measured with high *b* clinical DWI protocols. To do so, we employed Monte Carlo simulations of water diffusion in a synthetic tumor cell to study the signal dependence on cell diameter and nuclear volume fraction under a variety of experimental conditions.

METHODS

The tumor microenvironment is a complex milieu that includes not only cancer cells but also stromal cells,

[1]Department of Radiology, University of California, San Diego, La Jolla, California, USA.
[2]Department of Neuroscience, University of California, San Diego, La Jolla, California, USA.

Grant sponsor: National Institutes of Health; Grant numbers: R01AG031224, R01EB000790, RC2 DA29475, EB00790-06.

*Correspondence to: N. S. White, Multimodal Imaging Laboratory, Suite C101, 8950 Villa La Jolla Drive, La Jolla, CA 92037. E-mail: nswhite@ucsd.edu

Received 25 June 2013; revised 2 October 2013; accepted 20 October 2013
DOI 10.1002/mrm.25039
Published online 19 December 2013 in Wiley Online Library (wileyonlinelibrary.com).

inflammatory cells, and healthy cells. However, for the purpose of this study, we model the tumor microenvironment to consist of only cancer cells and extracellular space. As such, the total signal can be written as the sum of signals from the extracellular and intracellular (cancer cell) compartment weighted by their respective volume fractions:

$$S_{total} \approx f \cdot S_{intra} + (1 - f) \cdot S_{extra}, \quad [1]$$

where f is the volume fraction of cancer cells in the measured voxel. The main objective of this study was to investigate the nature of the intracellular restricted water signal S_{intra} obtained using clinically relevant experimental DWI parameters at high b. High b DWI offers greater sensitivity and specificity to the intracellular restricted water signal through intrinsic suppression (or filtering) of the relatively fast extracellular hindered water signal (S_{extra} in Equation 1). This greatly simplifies the diffusion model and simulation requirements as the effects of edema, necrosis, and extracellular space tortuosity can largely be ignored. In the first paragraph of the Results and Discussion section, we confirm the attenuation of S_{extra} at high b over a range of tortuosity factors.

Cancer Cell Simulation Model

Our cancer cell simulation model consisted a single three-dimensional spherical cell with a concentric spherical nucleus whose cellular (r_{cell}) and nuclear (r_n) radii were allowed to vary (Fig. 1). Each of the three compartments (intranuclear, cytoplasmic, and extracellular) was ascribed its own intrinsic diffusivity and transverse relaxation rate and separated by either an impermeable or semipermeable plasma membrane or highly permeable nuclear envelope. Specifically, for these initial simulations, we ascribed a plasma membrane permeability of either $P_{ce} = 0$ (impermeable) or $P_{ce} = 0.003$ μm/ms. The latter value was derived from prior experimental measurements of the intracellular/extracellular exchange rate for neural cells in intact functioning mammalian brains (10) using the permeability equation $1/P_{ce} = \tau_{ce}*(S/V)$ with $\tau_{ce} = 550$ ms and S/V corresponding to the surface-to-volume ratio of a 10 μm diameter spherical cell. The nuclear pore complex on the other hand allows for nearly free passage of water molecules between the nucleus and cytosol resulting in an effective exchange rate that is much higher than the plasma membrane (11,12). In order to emphasize the rapid exchange of water between the cytosol and nucleus, the nuclear membrane permeability was initially modeled as $P_{nc} = 0.5$ μm/ms, which corresponds to an average intranuclear residence time of approximately $\tau_{nc} = 1.65$ ms for a 5-μm diameter nucleus. However, it should be noted that so long as τ_{nc} remains short relative to the experimental diffusion time (i.e., fast exchange regime, $\tau_{nc} << \Delta$), the synthesized signal is relatively insensitive to the value for P_{nc}. To confirm this, we verified that the simulation results were nearly identical using $P_{nc} = 0.5$ μm/ms and the case of completely free exchange between the nucleus and cytosol, as others have modeled (13,14).

The lack of available experimental data makes it difficult to precisely model the intrinsic diffusion constants and relaxation rates for the nucleus and cytosol. Therefore, for this initial study, the following previously published parameters were used (13–16): nuclear diffusivity $D_n = 1.31$ μm^2/ms; cytoplasmic diffusivity $D_c = 0.48$ μm^2/ms; extracellular water diffusivity $D_{extra} = 1.0$ μm^2/ms; nuclear transverse relaxation $T2_n = 1/R2_n = 63.29$ ms; cytoplasmic transverse relaxation $T2_c = 1/R2_c = 23.87$ ms; and extracellular transverse relaxation $T2_{extra} = 1/R2_{extra} = 150$ ms. It should be noted that these parameters were measured in large ~0.5-mm single neurons isolated from *Aplysia californica* and therefore may not translate directly to tumor cells in vivo. To address this concern, we verified that the simulation results were robust to a broader range of parameter settings provided their relative values remained similar according to: D_{extra} and $D_n > D_c$, $T2_{extra}$ and $T2_n > T2_c$, and $\tau_{nc} << \Delta << \tau_{ce}$.

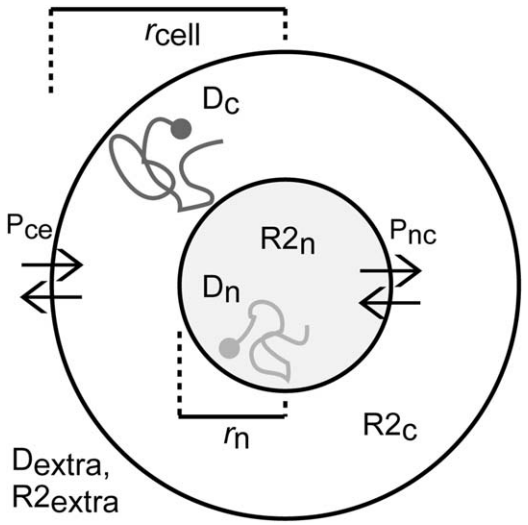

FIG. 1. Cancer cell simulation model. r_{cell} = cell radius (varied), r_n = nuclear radius (varied), D_c = cytosol diffusivity (fixed), D_n = nuclear diffusivity (fixed), $R2_c$ = cytosol transverse relaxation rate (fixed), $R2_n$ = nuclear transverse relaxation rate (fixed), D_{extra} = extracellular diffusivity (fixed), $R2_{extra}$ = extracellular transverse relaxation rate (fixed), P_{nc} = nuclear permeability (fixed), P_{ce} = plasma membrane permeability (varied).

Intracellular Signal Model

At ultra-short diffusion times, the diffusion length scales probed by intracellular spins are infinitesimal and the effects of restriction and exchange are negligible as the overwhelming majority of intracellular spins do not come in contact with the plasma or nuclear membrane. Under these experimental conditions, the cytosolic and nuclear compartment are not exchanging and the total intracellular signal for a single cancer cell is proportional to the superposition of signals from the two compartments:

$$S_{intra,short\,\Delta} \propto (1 - \nu) \cdot \underbrace{\exp(-TE \cdot R2_c) \cdot \exp(-b \cdot D_c)}_{S_{cytosol}} + \nu \cdot \underbrace{\exp(-TE \cdot R2_n) \cdot \exp(-b \cdot D_n)}_{S_{nucleus}}, \quad [2]$$

where $b = (\gamma\delta G)^2(\frac{\delta}{3} - \Delta)$ is the b-value of the experiment, γ is the gyromagnetic ratio for protons, G is the

amplitude the bipolar diffusion gradients with duration δ and separation Δ, respectively, TE is the echo time, and where $v \equiv (r_n/r_{cell})^3$ is the cell-wise nuclear volume fraction, as proportion of total intracellular volume. Note that in this study, we use cell-wise nuclear volume fraction v as opposed to nuclear-to-cytoplasm ratio (N/C ratio), as the latter is traditionally used to refer to the ratio of total nuclear to cytoplasmic (and extracellular) area using hematoxylin and eosin counterstaining.

On clinical scanners, however, the diffusion time is typically long relative to the average residence time of water molecules within the nucleus ($\Delta >> \tau_{nc}$), and the nucleus and cytosol are in fast exchange (fully mixed condition). To model this regime, we replaced the intrinsic diffusion constants and relaxation rates in Equation 2 by an apparent diffusion coefficient (ADC_{intra}) and apparent relaxation rate ($AR2_{intra}$). The intracellular diffusion signal for a tumor cell in the long diffusion time fast exchange regime then becomes:

$$S_{intra,long\,\Delta} \alpha \exp(-TE \cdot AR2_{intra}) \cdot \exp(-b \cdot ADC_{intra}). \quad [3]$$

ADC_{intra} in Equation 3 reflects the net displacement of intracellular water molecules during the diffusion time and is therefore a complex function of the plasma membrane permeability (exchange with the extracellular compartment) and the geometry of the intracellular compartment. $AR2_{intra}$, on the other hand, depends on the intrinsic instantaneous transverse relaxation rates of the intracellular fluid pools and the cumulative time spent by each spin in their respective compartments. Noting that in the fast exchange regime the cumulative time spent in each compartment is proportional to the volume fraction, the $AR2_{intra}$ in Equation 3 then becomes a simple function of the compartment-specific relaxation rates weighted by v:

$$AR2_{intra} = v \cdot R2_n + (1 - v) \cdot R2_c. \quad [4]$$

Simulation Details

Monte Carlo simulations (17–19) were used to evaluate the behavior of diffusing water molecules in our simplified cancer cell model and to generate synthetic intracellular diffusion signals under various experiment parameters. For each simulation run, 4×10^5 spins were assigned to random starting locations within the cell (initial x, y, z coordinates within the nucleus and cytosol) and then allowed to diffuse following a random walk model using their respective diffusivities and a temporal step size of 0.001 ms. At each time step, the spin phase vector in the transverse plane was updated according to the applied gradient field and the position of each spin within the field. To model restrictions and exchange, spins were reflected elastically off the contacted barrier (nuclear or plasma membrane) or allowed to pass through depending on the permeability constant. Intracellular spins that were selected to exchange through the plasma membrane had their phase replaced with those of randomly drawn simulated spins from the extracellular compartment. The extracellular spin phases were generated using separate simulation runs with identical experimental parameters, but no cells present. For all simulations, the gradient duration was set equal to the gradient separation ($\delta = \Delta$) to mimic the clinical setting. Furthermore, to ensure the simulated signals were independent of starting location and the path history of each spin, each simulation run was repeated several times, and plots were verified to be essentially identical. All simulations were performed in house using MATLAB (Mathworks, Inc, Natick, Massachusetts, USA) running on a Dell workstation with a quad-core 2.67 GHz Intel Xeon X5550 Processor with 48 GB of RAM.

RESULTS

Attenuation of the Extracellular Water Signal at High b

Figure 2a plots the relative sensitivity of S_{total} to S_{extra} in terms of the ratio S_{extra}/S_{intra} as a function of b. For these plots, S_{extra} was generated analytically using the formula $S_{extra} = \exp(-TE \cdot AR2_{extra}) \cdot \exp(-b \cdot ADC_{extra})$ with $ADC_{extra} = 1.0$ $\mu m^2/ms$ and $AR2_{extra} = 1/150$ ms, while S_{intra} was simulated with the following parameters: $v = 0.8$; cell diameter $= 10$ μm; $P_{ce} = 0.003$ $\mu m/ms$ $TE = 140$ ms; $\Delta = 60$ ms. As demonstrated in the figure, the contribution of S_{extra} to the total signal decays rapidly as a function of b and is negligible at $b = 4000$ s/mm^2. This is true even when taking into account the predicted changes in ADC_{extra} due to changing extracellular space tortuosity λ with volume fraction α. Note that the high and low α regime plotted in Figure 2a was derived from Figure 7 of Chen and Nicholson (20) (reprinted in Fig. 2b) which plots empirical and theoretical values for λ as a function of α under sever osmotic stress conditions. Specifically, for the high and low α regime, we modulated ADC_{extra} by a factor of 1.13 and 0.88, respectively, which was derived from the ratio of λ^2 values in Figure 2a. As a reference, the case of vasogenic edema in the tumor extracellular space is also plotted in Figure 2a with elevated $ADC_{extra} = 2.7$ $\mu m^2/ms$ and reduced $AR2_{extra} = 1/500$ ms.

Effects of Cell Diameter on S_{intra}

Figure 3 demonstrates the change in the intracellular restricted water signal S_{intra} with cell diameter at $b = 4000$ s/mm^2 over a range of diffusion times Δ and with nuclear volume fraction fixed. Also shown are the corresponding estimated values of $AR2_{intra}$ and ADC_{intra} fit to the simulated signal according to Equation 3. Note the change in S_{intra} with cell diameter is more pronounced at short diffusion times, but at long (clinically relevant) diffusion times the signal dependence on cell diameter is minimal (Fig. 3A). Also note that the cause of the slight decrease in S_{intra} with increasing cell diameter at long diffusion times is an increase in ADC_{intra} for larger cells (Fig. 3C black lines), while $AR2_{intra}$ remains constant (Fig. 3B), as expected, being only a function of v (Eq. 4). Figure 3D demonstrates that a similar dependence in S_{intra} with cell diameter is observed when allowing for exchange with the extracellular compartment.

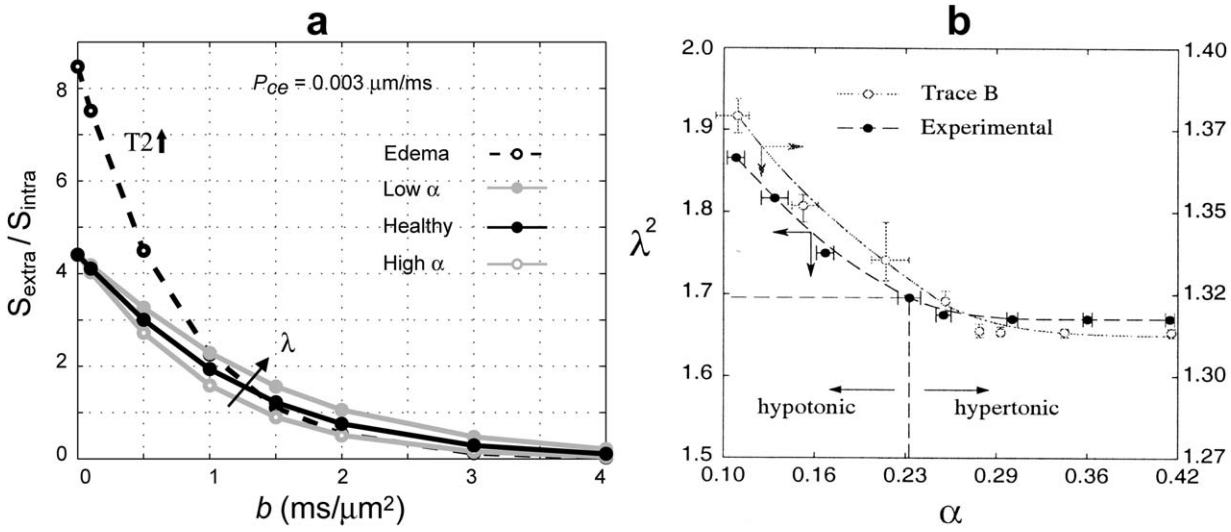

FIG. 2. Reduced sensitivity to extracellular water at high *b*. **a:** Ratio of S_{extra} / S_{intra} as a function of *b* demonstrating negligible contribution of the extracellular water signal to the total signal at $b = 4000$ s/mm^2. This is true even when taking into account the predicted change in ADC_{extra} due to changing extracellular space tortuosity λ with volume fraction α. **b:** Theoretical and experimental λ versus α plots [reprinted with permission from Chen and Nicholson (20)] from which the high and low α curves were derived and plotted in panel a.

Effects of Nuclear Volume Fraction on S_{intra}

Figure 4 demonstrates the change in the intracellular restricted water signal S_{intra} with nuclear volume fraction *v* at $b = 4000$ s/mm^2 over a range of diffusion times Δ and with cell diameter fixed. Also shown are the corresponding estimated values of $AR2_{intra}$ and ADC_{intra} fit to the simulated signal according to Equation 3. Notice here that the change in S_{intra} is exponential in *v* and is maximal at long (clinically relevant) diffusion times. Also, notice the cause of the exponential increase in signal with *v* is a corresponding linear decrease in $AR2_{intra}$ (Fig. 4B) as expected from Equation 4, whereas ADC_{intra} remains relatively constant (Fig. 4C). Note that the slight decrease in ADC_{intra} with *v* at long diffusion time may be explained by the increased probability of intracellular spins reflecting off the nuclear membrane, thereby reducing the effective pore size experience by each spin. Notice also that a similar exponential increase in signal with *v* is observed when allowing for exchange with the extracellular compartment (Fig. 4D).

DISCUSSION

The goal of this study was to investigate the specific effect of cell diameter and nuclear volume fraction on clinical DWI contrast of tumors at high *b*. We found that traditional pulsed-gradient spin echo diffusion-weighted signals at high *b*, long diffusion time, and long echo time were relatively insensitive to cell diameter over a physiologically relevant range, but increased exponentially with the nuclear volume fraction of individual tumor cells.

At first, our results demonstrating a strong dependency of high *b* clinical DWI contrast to cell-wise nuclear volume fraction (*v*) seems at odds with the findings of Xu et al. (14), who observed limited or no sensitivity to *v* by traditional pulsed-gradient diffusion measures and greater sensitivity to *v* when sampling over a range of short diffusion times using oscillating gradients. However, it should be noted that although the Xu et al. study used diffusion parameters identical to those in the current study (i.e., $D_n = 1.31$ μm^2/ms, cytoplasm $D_c = 0.48$ μm^2/ms), they assumed the intracellular T2 was homogenous everywhere (i.e., $R2_n = R2_c$), which obviously removes the T2 effect. Furthermore, the comparisons in the Xu et al. study were performed at low *b* ($b = 1$ ms/μm^2) and short echo time (TE = 40 ms), which also reduces sensitivity to T2 differences of intracellular water. Taken together, the results of this study suggest that although oscillating-gradient measures at low *b*, short TE, and short diffusion time appear sensitive to changes in *v* through compartmental differences in diffusivity but not T2, clinical pulsed-gradient diffusion measurements at high *b*, long TE, and long diffusion time appear sensitive to changes in *v* through compartmental differences in T2 but not diffusivity.

Compartmental T2 Filtering and Cellular Conspicuity Factor

It is important to recall that diffusion signals are intrinsically dual-filtered by both the *b*-value and echo time of the experiment and that although traditional ADC removes the effect of bulk tissue T2 on the diffusion estimate by normalizing with respect to the signal at $b = 0$, compartmental differences in T2 still cause a differential weighting of the respective water pools to the measured signal and ADC at long echo time. We demonstrate in this study that when the nucleus and cytosol are in fast exchange, the effective T2 for the intracellular compartment increases linearly with nuclear volume fraction causing cells with large *v* to be weighted more to the measured signal and ADC compared with cells with small *v* (Fig. 4). Moreover, the weighting that is exponential with *v* can be quantified by substituting Equation 4 into Equation 3 resulting in:

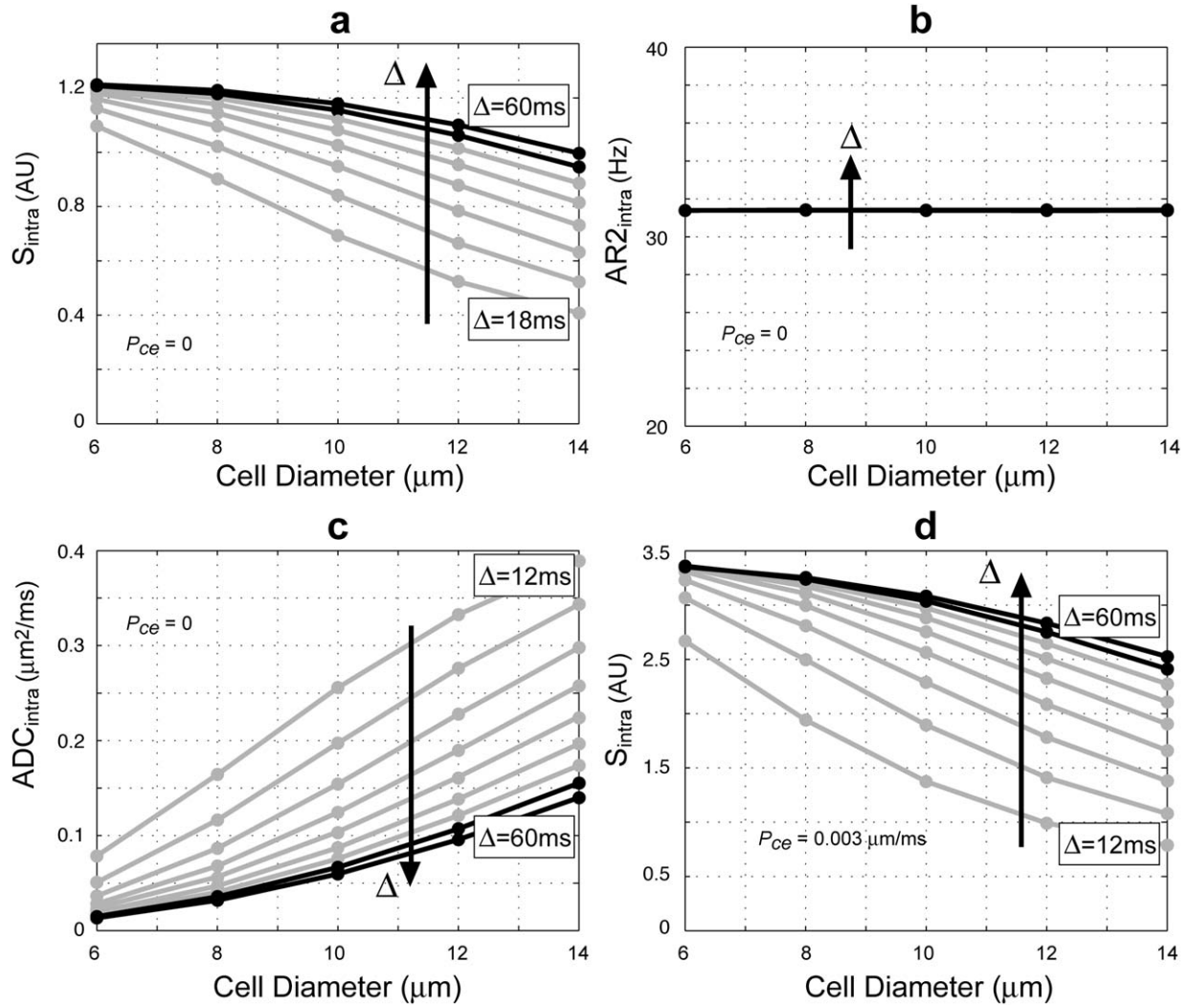

FIG. 3. Simulated S_{intra} as a function of cell diameter (i.e., $2 \cdot r_{cell}$). **a:** S_{intra} with no exchange ($P_{ce} = 0$) and corresponding fitted values for (**b**) $AR2_{intra}$ and (**c**) ADC_{intra}. **d:** S_{intra} allowing for exchange with the extracellular compartment $P_{ce} = 0.003$ μm/ms. Simulation parameters: $v = 0.4$, $b = 4000$ s/mm^2, TE = 140 ms, $\delta = \Delta = [12,18,24,30,36,42,48,54,60]$ ms. Black lines indicate clinically relevant parameters.

$$S_{intra} \propto \exp(-b \cdot ADC_{intra}) \cdot \kappa(v), \quad [5]$$

where

$$\kappa(v) = \exp(-TE \cdot [v \cdot R2_n + (1 - v) \cdot R2_c]) \quad [6]$$

We refer to κ in Equation 6 as the "cellular conspicuity factor" because it describes the relative contribution of individual cells (or collections of cells with similar properties) to the measured intracellular signal at high b. Note that Equation 5 can be simplified further by noting that ADC_{intra} is independent of both diameter and v and low at long diffusion time due to restriction effects with the plasma membrane (Fig. 4), resulting in

$$S_{intra} \propto \kappa(v) \quad [7]$$

as $\exp(-b \cdot ADC_{intra}) \sim 1$. The concept of dual filtering with b and TE together with plots of the cellular conspicuity factor κ is provided in Figure 5.

Predicted Voxel-Level Signal

The majority of this study focused on understanding and characterizing signals from individual cancer cells or collections of cells with identical properties. However, it is fairly straightforward to extrapolate to the case of a tumor voxel containing a distribution of cancer cells with varying nuclear volume fractions. To do so, we need to integrate Equation 7 over a distribution of v such that the predicted tumor signal at high b and long Δ becomes

$$S_{tumor} \propto \int \kappa(v) f(v) dv, \quad [8]$$

where $f(v)$ describes the proportion of total volume taken up by cells with a given v. Although Equation 8 applies to any arbitrary distribution of nuclear volume fractions, assume for the moment that $f(v)$ follows a raised cosign function with finite support over the interval $[a = \mu - s, b = \mu + s]$ such that:

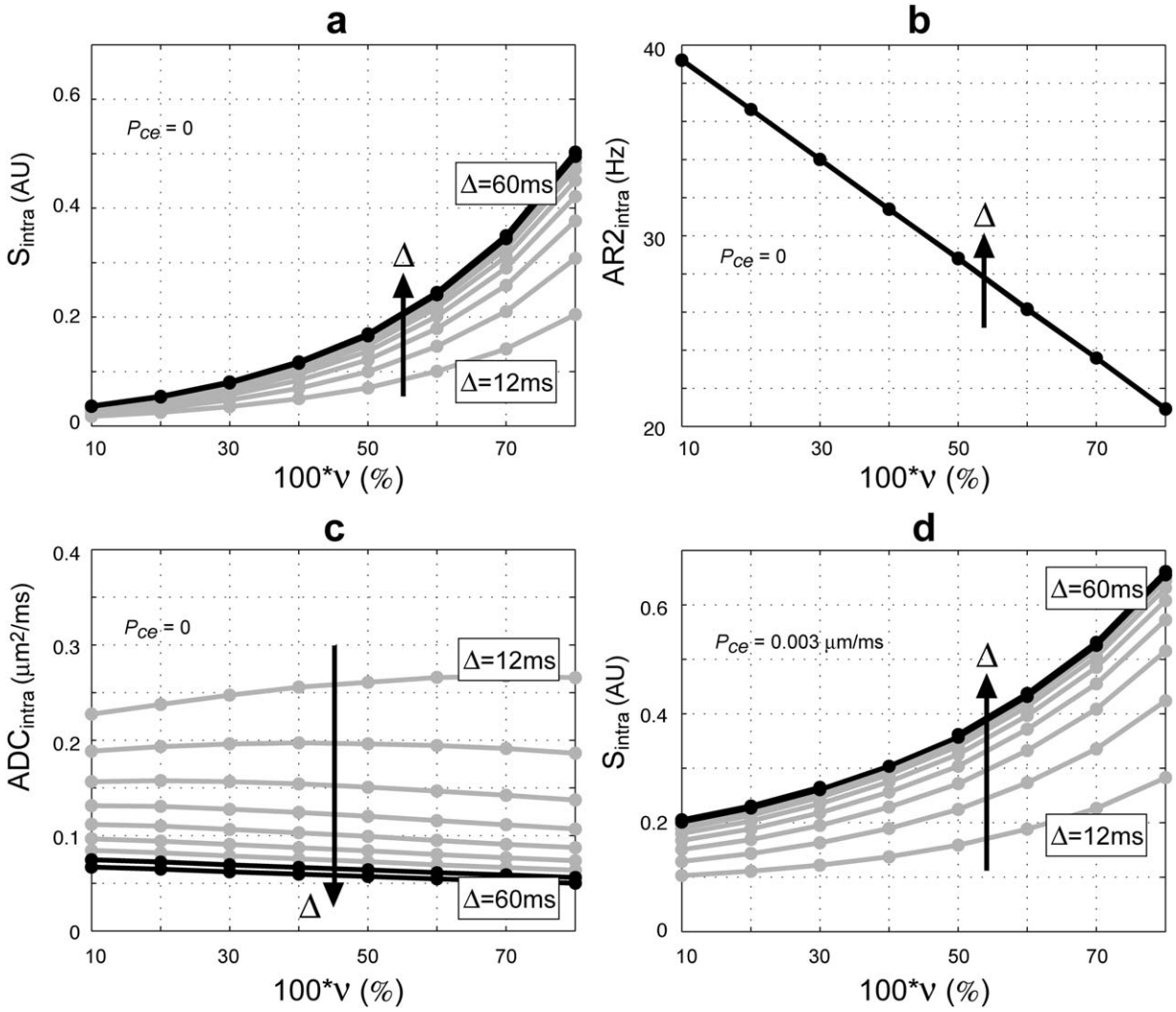

FIG. 4. Simulated S_{intra} as a function of v. **a:** S_{intra} with no exchange ($P_{ce} = 0$) and corresponding fitted values for (**b**) $AR2_{intra}$ and (**c**) ADC_{intra}. **d:** S_{intra} allowing for exchange with the extracellular compartment $P_{ce} = 0.003$ μm/ms. Simulations parameters: cell diameter = 10 μm, $b = 4000$ s/mm^2, TE = 140 ms, $\delta = \Delta = [12,18,24,30,36,42,48,54,60]$ ms. Black lines indicate clinically relevant parameters.

$$f(x;\mu,s) = \frac{1}{2s}\left[1 + \cos\left(\frac{x-\mu}{s}\pi\right)\right]. \quad [9]$$

Then the solution to the integral equation for the predicted voxel-level signal in tumor is given by the following closed form expression:

$$S_{\text{tumor}}\,\alpha\, -\frac{\pi^2}{2}\left[\frac{e^{TE\cdot\{R2_c(a-1)-R2_n(a)\}} - e^{TE\cdot\{R2_c(b-1)-R2_n(b)\}}}{(R2_c - R2_n)\cdot s\cdot TE\cdot(\pi^2 + (R2_c - R2_n)^2\cdot s^2\cdot TE^2)}\right]. \quad [10]$$

Note that the signal increases monotonically with both the mean μ and dispersion s of the intravoxel distribution of nuclear volume fraction v.

Clinical Relevance: Revisiting the ADC/Cellularity Relation at Low *b*

In clinical practice, tumor ADC values are traditionally calculated using monoexponential analysis of the diffusion-weighted signal decay over a relatively low b value range of around 1000 s/mm^2. For the purpose of this discussion, we refer to the traditional low b value ADC as ADC_{total} to distinguish this quantity from ADC_{intra} that was calculated using Equation 3 at high b values ($\sim$ 4000 s/mm^2) and is presented in Figures 3 and 4. Several studies have documented a negative correlation between tumor cell density (cellularity) and ADC_{total} (21–25), yet this relationship does not generalize across all tumor categories. For example, schwannomas and oligoastrocytomas are tumors with relatively high cell density, which would imply elevated restriction diffusion and, accordingly, low ADC_{total}; however, they exhibit comparatively high diffusion coefficients (1,26). Although heterogeneity of tissue and partial voluming of vasogeneic edema may explain in part the high diffusion coefficient of these tumors, our results suggest another factor could be at play that has not been considered previously. Specifically, the results of this study suggest that high ADC_{total} measured in these tumors may result from the abundance of cells with relatively low nuclear

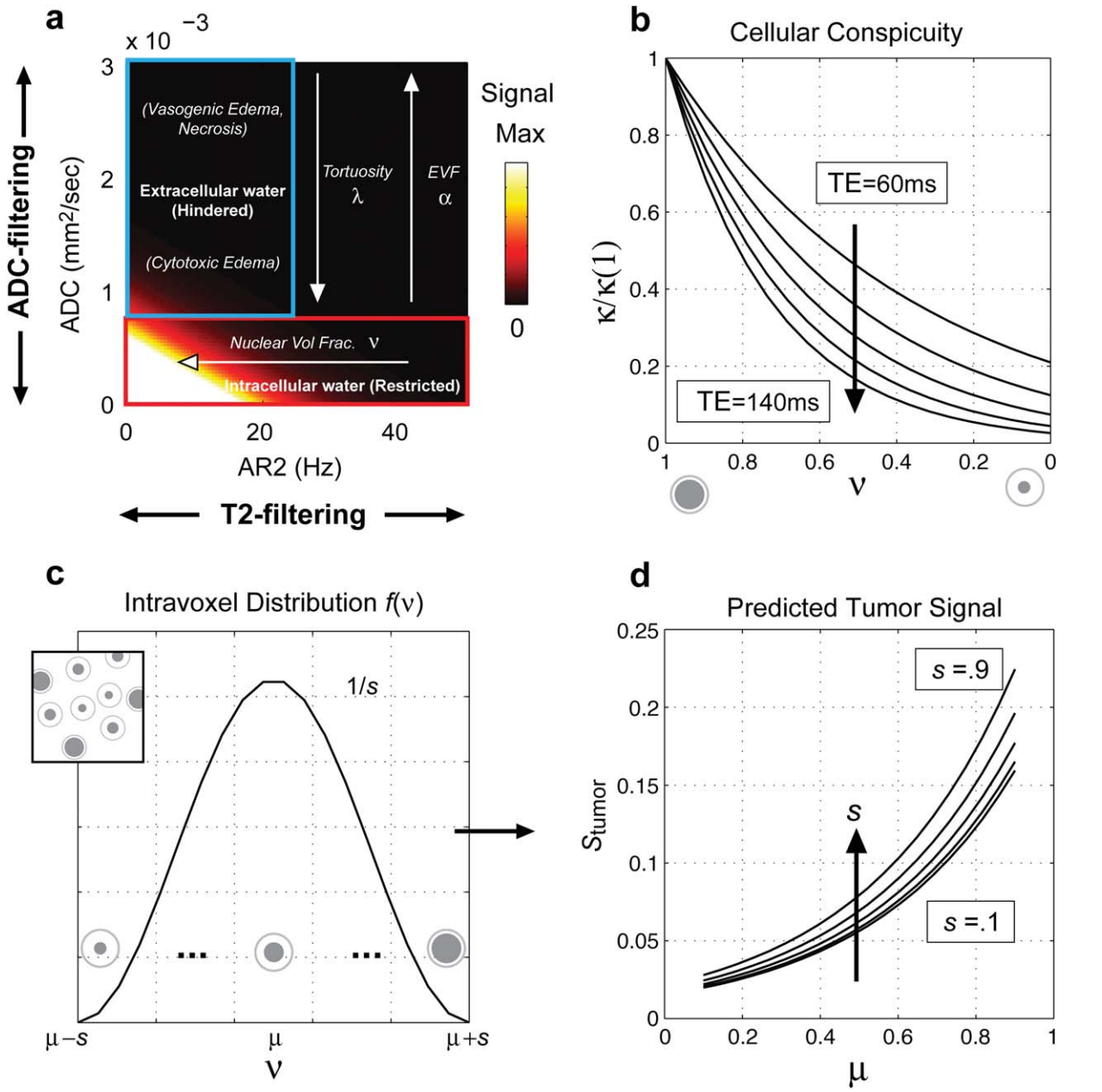

FIG. 5. **a**: DWI data are dual-filtered along ADC and AR2 depending on the *b*-value and echo time, respectively. At high *b* and long Δ, water from the fast extracellular compartment is attenuated providing intrinsic selection of slow intracellular restricted water. Similarly, at long TE, cell populations with low T2 (high AR2) are attenuated providing intrinsic selection of cells with high T2 (low AR2). **b:** Plots of the cellular conspicuity factor κ at different TEs [60,80,100,120,140 ms] quantifying the exponential T2 filtering of cells with decreasing ν (see Eq. 6). **c:** A raised cosign function for the intravoxel nuclear volume fraction distribution $f(\nu)$ leads to (**d**) an analytic expression for the predicted voxel-level signal in tumors, which depends on both the mean μ and dispersion s [.1,.3,.5,.7,.9 shown] of the nuclear volume fraction distribution (Eqs. 8–10).

volume fractions. As the tumor cell nuclei decrease in size relative to their respective diameters, the effective T2 of intracellular water decreases (Fig. 4b), causing a decrease in the relative weighting of the slow intracellular restricted water fraction (low ADC_{intra}, Fig. 4c) on the measured diffusion-weighted signal at long echo time (Fig. 4a). Accordingly, ADC_{total} will be elevated due to a stronger relative weighting of the fast extracellular hindered fraction (ADC_{extra}) in these tumors. On the other hand, the low ADC_{total} of tumors composed of cells with large nuclear volume fractions (e.g., glioblastomas and lymphomas) may result from a stronger relative weighting of the slow intracellular restricted pool versus the fast extracellular hindered pool. Interestingly, the study of Gauvain et al. (25), demonstrated a stronger correlation of ADC_{total} with total nuclear area of tumors compared with total cellular area, which is consistent with this result. Moreover, we have noticed in our own work,

using a technique known as Restriction Spectrum Imaging (RSI) (6,27–29), that the magnitude of the intracellular restricted signal at high *b* values appears to be modulated by both cell density and nuclear volume fraction of individual cells, although further work is required to validate this observation using quantitative stereology techniques.

Future Directions

Many advanced DWI techniques are emerging to better characterize and model water compartmentalization and complex diffusion in tissues on clinical scanners such as diffusion kurtosis imaging (30) and RSI (29). Our results here suggest that by manipulating echo time and *b*-value, it may be possible to further decompose the diffusion into proportions of water that can be attributed to cells with small versus large nuclear volume fractions. Moreover, the high intrinsic contrast to cells with large nuclei at high *b* and long echo time should in principle enable improved detection of even small populations of highly malignant tumor cells. Finally, given that a characteristic feature of many stem cells is high nuclear volume fractions, these techniques may also hold promise for noninvasive stem cell tracking applications without the need for extrinsic contrast agent, although the concentration limits and scan time requirements required for sufficient diffusion contrast remains to be determined and should be compared with established techniques.

CONCLUSION

In this study, we derive a simple analytic expression for the diffusion signal within tumors capturing the effect of tumor cell density and cell-wise nuclear volume fraction (v) on clinical DWI data. We show how the intracellular restricted water signal measured with traditional pulsed-gradient spin-echo acquisitions at high *b* and with long diffusion times and long echo times is relatively insensitive to the size of individual tumor cells, but increases exponentially with v. Moreover, we provide a mathematic framework to validate the MRI-derived histological parameters directly against empirically derived distributions of nuclear volume fractions of individual cells, which may be obtained, for example, stereological methods applied to histological data that stain for both plasma and nuclear membranes. The model, which is based on compartmental differences in T2 between the nucleus and cytosol, may help explain the additional variation in DWI signal and traditional ADC at low *b* ($\sim$1000 s/mm^2) within and across different tumor types that cannot be explained on the basis of cell density alone. Specifically, our model predicts that at long echo times, a component of reduced ADC in some tumors may be due to a greater weighting on the intracellular restricted water fraction for cells with larger nuclei due to the reduced apparent R2 (higher T2) for intracellular water in these cells. Conversely, the elevated ADC in some cell-rich tumors may be due to a reduced weighting on the intracellular restricted water fraction for cells with smaller nuclei and a greater relative weighting of the fast extracellular water fraction in these tumors.

ACKNOWLEDGMENTS

We would like to thank the patients at the University of California, San Diego Neuro-Oncology Program for their generous participation.

REFERENCES

1. Maier SE, Sun Y, Mulkern RV. Diffusion imaging of brain tumors. NMR Biomed 2010;23:849–864.
2. Sykova E, Nicholson C. Diffusion in brain extracellular space. Physiol Rev 2008;88:1277–1340.
3. Pfeuffer J, Flogel U, Dreher W, Leibfritz D. Restricted diffusion and exchange of intracellular water: theoretical modelling and diffusion time dependence of 1H NMR measurements on perfused glial cells. NMR Biomed 1998;11:19–31.
4. Le Bihan D. Molecular diffusion, tissue microdynamics and microstructure. NMR Biomed 1995;8:375–386.
5. Seo HS, Chang KH, Na DG, Kwon BJ, Lee DH. High b-value diffusion (b = 3000 s/mm2) MR imaging in cerebral gliomas at 3T: visual and quantitative comparisons with b = 1000 s/mm^2. AJNR Am J Neuroradiol 2008;29:458–463.
6. White NS, McDonald CR, Farid N, Kuperman JM, Kesari S, Dale AM. Improved conspicuity and delineation of high-grade primary and metastatic brain tumors using restriction spectrum imaging: quantitative comparison with high B-value DWI and ADC. AJNR Am J Neuroradiol 2013;34:958–964
7. Alvarez-Linera J, Benito-Leon J, Escribano J, Rey G. Predicting the histopathological grade of cerebral gliomas using high b value MR DW imaging at 3-tesla. J Neuroimaging 2008;18:276–281.
8. Doskaliyev A, Yamasaki F, Ohtaki M, et al. Lymphomas and glioblastomas: differences in the apparent diffusion coefficient evaluated with high b-value diffusion-weighted magnetic resonance imaging at 3T. Eur J Radiol 2012;81:339–344.
9. Edens LJ, White KH, Jevtic P, Li X, Levy DL. Nuclear size regulation: from single cells to development and disease. Trends Cell Biol 2013; 23:151–159.
10. Quirk JD, Bretthorst GL, Duong TQ, Snyder AZ, Springer CS Jr, Ackerman JJ, Neil JJ. Equilibrium water exchange between the intra- and extracellular spaces of mammalian brain. Magn Reson Med 2003; 50:493–499.
11. Maul GG, Deaven L. Quantitative determination of nuclear pore complexes in cycling cells with differing DNA content. J Cell Biol 1977; 73:748–760.
12. Allen TD, Cronshaw JM, Bagley S, Kiseleva E, Goldberg MW. The nuclear pore complex: mediator of translocation between nucleus and cytoplasm. J Cell Sci 2000;113:1651–1659.
13. Xu J, Does MD, Gore JC. Dependence of temporal diffusion spectra on microstructural properties of biological tissues. Magn Reson Imaging 2011;29:380–390.
14. Xu J, Does MD, Gore JC. Sensitivity of MR diffusion measurements to variations in intracellular structure: effects of nuclear size. Magn Reson Med 2009;61:828–833.
15. Grant SC, Buckley DL, Gibbs S, Webb AG, Blackband SJ. MR microscopy of multicomponent diffusion in single neurons. Magn Reson Med 2001;46:1107–1112.
16. Schoeniger JS, Aiken N, Hsu E, Blackband SJ. Relaxation-time and diffusion NMR microscopy of single neurons. J Magn Reson B 1994;103:261–273.
17. Szafer A, Zhong J, Gore JC. Theoretical model for water diffusion in tissues. Magn Reson Med 1995;33:697–712.
18. Hall MG, Alexander DC. Convergence and parameter choice for Monte-Carlo simulations of diffusion MRI. IEEE Trans Med Imaging 2009;28:1354–1364.
19. Regan DG, Kuchel PW. Simulations of NMR-detected diffusion in suspensions of red cells: the effects of variation in membrane permeability and observation time. Eur Biophys J 2003;32:671–675.
20. Chen KC, Nicholson C. Changes in brain cell shape create residual extracellular space volume and explain tortuosity behavior during osmotic challenge. Proc Natl Acad Sci U S A 2000;97:8306–8311.
21. Uhl M, Altehoefer C, Kontny U, Il'yasov K, Buchert M, Langer M. MRI-diffusion imaging of neuroblastomas: first results and correlation to histology. Eur Radiol 2002;12:2335–2338.
22. Sugahara T, Korogi Y, Kochi M, et al. Usefulness of diffusion-weighted MRI with echo-planar technique in the evaluation of cellularity in gliomas. J Magn Reson Imaging 1999;9:53–60.

23. Rodallec M, Colombat M, Krainik A, Kalamarides M, Redondo A, Feydy A. Diffusion-weighted MR imaging and pathologic findings in adult cerebellar medulloblastoma. J Neuroradiol 2004;31:234–237.
24. Gupta RK, Cloughesy TF, Sinha U, Garakian J, Lazareff J, Rubino G, Rubino L, Becker DP, Vinters HV, Alger JR. Relationships between choline magnetic resonance spectroscopy, apparent diffusion coefficient and quantitative histopathology in human glioma. J Neurooncol 2000;50:215–226.
25. Gauvain KM, McKinstry RC, Mukherjee P, Perry A, Neil JJ, Kaufman BA, Hayashi RJ. Evaluating pediatric brain tumor cellularity with diffusion-tensor imaging. AJR Am J Roentgenol 2001;177: 449–454.
26. Yamasaki F, Kurisu K, Satoh K, et al. Apparent diffusion coefficient of human brain tumors at MR imaging. Radiology 2005;235: 985–991.
27. Kothari PD, White NS, Farid N, Chung R, Kuperman JM, Girard HM, Shankaranarayanan A, Kesari S, McDonald CR, Dale AM. Longitudinal restriction spectrum imaging is resistant to pseudoresponse in patients with high-grade gliomas treated with bevacizumab. AJNR Am J Neuroradiol 2013;34:1752–1757.
28. McDonald CR, White NS, Farid N, et al. Recovery of white matter tracts in regions of peritumoral FLAIR hyperintensity with use of restriction spectrum imaging. AJNR Am J Neuroradiol 2013;34:1157–1163.
29. White NS, Leergaard TB, D'Arceuil H, Bjaalie JG, Dale AM. Probing tissue microstructure with restriction spectrum imaging: histological and theoretical validation. Hum Brain Mapp 2013;34:327–346.
30. Jensen JH, Helpern JA, Ramani A, Lu H, Kaczynski K. Diffusional kurtosis imaging: the quantification of non-gaussian water diffusion by means of magnetic resonance imaging. Magn Reson Med 2005;53: 1432–1440.